Ceramics International 51 (2025) 44619–44632

Contents lists available at ScienceDirect

Ceramics International

journal homepage: www.elsevier.com/locate/ceramint

Defects, microstructural, optical, and electrical evolution of NiO nanostructured thin films by 0.2 MeV/u C^+ ion irradiation

Dineo P. Sebuso [a,*], Cosmas Muiva [a], Othmane Mouane [b], Rudolph M. Erasmus [b], Morgan Madhuku [c], Elias Sideras-Haddad [b,d]

[a] Department of Physics and Astronomy, Botswana International University of Science and Technology, Private Bag 16, Palapye, Botswana
[b] Material Physics Research Institute, School of Physics, University of the Witwatersrand, Wits, 2050, Johannesburg, South Africa
[c] iThemba LABS, Tandem and Accelerator Mass Spectrometry Department, Private Bag 11, Johannesburg, 2050, South Africa
[d] Department of Industrial Design and Production Engineering, School of Engineering-University of West Attica, Greece

ARTICLE INFO

Handling Editor: Dr P. Vincenzini

Keywords:
Ion irradiation
NiO nanostructured thin films
Electronic energy loss
Localized defects
Rietveld refinement

ABSTRACT

The current study unveils the impact of 2.4 MeV C^+ ion irradiation on the microstructure, optical properties, and electrical evolution of NiO nanostructured thin films at various fluences from 2×10^{13} to 1×10^{15} ions/cm^2. The NiO nanostructured thin films were deposited on glass substrates via an easy and efficient spray pyrolysis method. X-ray diffraction (XRD) and Raman spectroscopy have been used to study the structural defects and lattice distortion induced in the irradiated samples. The Rietveld refinement technique of XRD data revealed variations in crystallite size due to the irradiation. A slight increase in the energy band gap of pristine NiO from 3.24 eV to 3.29 eV is observed at low C^+ ion fluence (2×10^{13} ions/cm^2), followed by a notable decrease to 2.80 eV at high fluence (1×10^{15} ions/cm^2). A similar trend is observed with the Urbach energy (E_u). Moreover, the electronic energy loss led to higher conductivity, from 9.83 $\Omega^{-1}m^{-1}$ for pristine NiO to 12.70 $\Omega^{-1}m^{-1}$ for carbon-irradiated NiO at a fluence of 1×10^{15} ions/cm^2. The results reveal that carbon ion irradiation induces electronic excitation and ionization, generating localized defects, microstructural evolution, tailored optical absorption, and enhanced electrical conductivity in NiO, expanding its use in various applications.

1. Introduction

Interactions between accelerated ions approaching the atoms of a solid target, before and upon impact, induce significant transformation within the target material. Such atomic collisions in solids induce changes with respect to structural, magnetic, optical, and electrical properties of materials [1–3]. In this manner, ion beams are being utilized in the engineering of nanostructures and modern electro-optical devices [4–6]. As the energetic ion traverses a target, it loses its kinetic energy via two mechanisms: nuclear energy loss and electronic energy loss. Nuclear energy loss (S_n) occurs in a low-ion energy regime, where atoms are displaced, defects are generated, and ion implantation occurs [7,8]. The electronic energy loss (S_e) mechanism is based on intensive electronic excitations and ionization of the atoms of the target material. The result of such energy losses is the formation of point defects and dislocations [9–11]. Radiation effects induced in this way depend on several factors, such as fluence, incoming ion energy, and the atomic number of the irradiating ions. Many different research studies have shown the use of ion beams to enhance the properties of transition metal oxides. Xia et al. [12], used 50 keV N^+ ion irradiation to improve the conductivity of NiO nanosheets for enhanced oxygen evolution reaction electrocatalytic performance. Tripathi et al. [13] reported on the engineering of NiO thin film properties through silver ion irradiation. This led to an improvement in the crystallite size of NiO thin films irradiated with lower ion fluence, alterations in surface morphology, and an increase in surface roughness with higher ion fluence. Li et al. [14] induced defects in the crystal structure of NiO through He^+ ion irradiation, which also reduced the thickness of the NiO nanosheets, resulting in higher-surface-area structures optimized as catalysts with enhanced oxygen evolution reaction (OER) performance. Bhakta et al. [15] reported that defects introduced by 30 keV Au ions resulted in variations in crystallite size and band gap narrowing. Mishra et al. [16] investigated the influence of 1.2 MeV argon ion irradiation on the magnetic properties of ZnO. Their results revealed that unirradiated ZnO with a diamagnetic ordering transform to ferromagnetic behaviour post-irradiation due to the formation of stable defects.

* Corresponding author.
E-mail address: dsebuso@gmail.com (D.P. Sebuso).

https://doi.org/10.1016/j.ceramint.2025.07.190
Received 5 December 2024; Received in revised form 29 June 2025; Accepted 15 July 2025
Available online 18 July 2025

This study investigates the effects of irradiation-induced defects on the microstructure, optical properties, and electrical evolution of NiO nanostructured thin films. Ion irradiation provides a controlled approach to defect engineering [17–19], enabling the modification or enhancement of specific properties to make NiO suitable for sensors, optoelectronics, and transparent electronic applications. Therefore, it is crucial to investigate how energetic ions impact NiO thin films. This research specifically focuses on the response of NiO nanostructured thin films to MeV heavy ion irradiation, emphasizing modifying electronic properties for advanced applications. These modifications can be particularly useful for sensor development in reactor environments and optoelectronic devices.

Nanostructured thin films possess distinctive physical, chemical, and structural properties due to their nanoscale aspect and high surface area-to-volume ratios [20]. Their special features can be tuned to fulfil specific requirements, creating a vast array of applications in numerous fields. NiO is one of the most intensively studied transition metal oxides due to its intrinsic properties, such as a broad band gap, transparency in the Vis-NIR [21], p-type carrier concentration, and elevated electron mobility [5,22]. These properties enable NiO to be utilized in various applications, including photovoltaic solar cells [23], optical power limiters [24], magnetic storage devices [25], gas sensors [26], batteries [27], and catalysis [28]. Different techniques have been used for the fabrication of NiO nanostructured thin films, such as radio frequency reactive magnetron sputtering [29], co-doped NiO by the sol-gel method [30], reactive-pulsed laser ablation technique [31], electrodeposition [32], mist chemical vapour deposition [33], and the spray pyrolysis method [34,35]. Compared to other methods, spray pyrolysis offers numerous benefits, including inexpensive costs, basic deposition equipment, easy composition regulation [36], and particle size.

In this work, NiO nanostructured thin films with a thickness of the order of 800 nm, were bombarded with 2.4 MeV C^+ ions equivalent to 0.2 MeV/u C^+ ions at various fluences. The Stopping and Range of Ions in Matter (SRIM) Monte Carlo simulation code was used to provide insight into the irradiation damage due to the incident ions. This study focuses on radiation damage solely to electronic energy loss and not nuclear stopping. In this regard, any potential effects of carbon dopants from the incoming ions were excluded. Therefore, special care was taken to select carbon bombardment energies that traverse the film and stop at the substrate. To the best of our knowledge, no research has been done on C^+ ion-irradiated NiO nanostructured thin films. This research will shed light on the relationship between irradiation-induced lattice defects, optical and electrical properties of NiO for optoelectronic applications.

2. Experimental

2.1. Synthesis of NiO nanostructured thin films

A simple spray pyrolysis setup, displayed in Fig. 1, was used to deposit NiO thin films on a glass substrate. The glass substrates were initially cleaned using dilute nitric acid and ethanol, followed by distilled water for 15 min in each solvent through ultrasonication. The glass substrates were further rinsed with distilled water and blown with dry air. 0.1 M of nickel (ii) nitrate hexahydrate was dissolved in distilled water and magnetically stirred for 30 min. The aqueous nickel nitrate hexahydrate, of volume of 15 ml, was sprayed on the preheated glass slides at a flow rate of 0.25 ml/min under compressed air to form a thin film. The spraying temperature was maintained at 450 °C. The spray nozzle and glass substrates were separated at a fixed distance of 29.5 cm. The glass substrates were left on the hotplate for 30 min after the deposition process to evaporate residual solvents. The thin films were then annealed at a temperature of 450 °C for 30 min. The thickness of the NiO nanostructured thin films was determined using a mechanical scanning technique called the Tencor stylus profilometer. Measurements were taken several times across different areas of the film, yielding values ranging from 797 to 803 nm. The average was then calculated and rounded to the nearest significant figure, resulting in a thickness of 800 nm. The fabricated NiO thin films were regarded as nanostructured due to the nanoscale dimensions of the grains composing the film.

2.2. Ion irradiations

The thin films were subsequently cut into small pieces measuring 5 mm by 5 mm. The films were then irradiated with C^+ ions using the 6 MV EN Tandem accelerator at iThemba LABS, Johannesburg, South Africa. The target was irradiated at room temperature under vacuum with a beam current of approximately 20 nA, and the ion fluence was varied by changing the exposure time. The NiO nanostructured thin films were irradiated with a beam energy of 2.4 MeV C^+ ions using different fluences (number of ions/cm^2) of 2×10^{13}, 1×10^{14}, 2×10^{14}, and 1×10^{15} ions/cm^2. The energy of 2.4 MeV was chosen to ensure that the ion beam traverses the thin film without stopping within it. In this way, it was assured that the defects due to only electronic stopping were induced. The SRIM simulations of ion-solid interactions were performed and are displayed in Fig. 2. After ion irradiation, the NiO nanostructured thin films were characterized using various techniques, without any post-treatment.

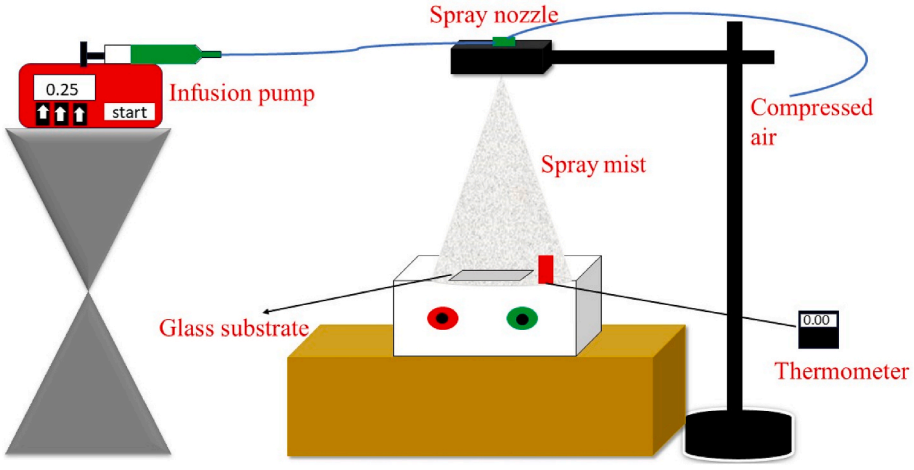

Fig. 1. The spray pyrolysis set up used for the deposition of NiO nanostructured thin films.

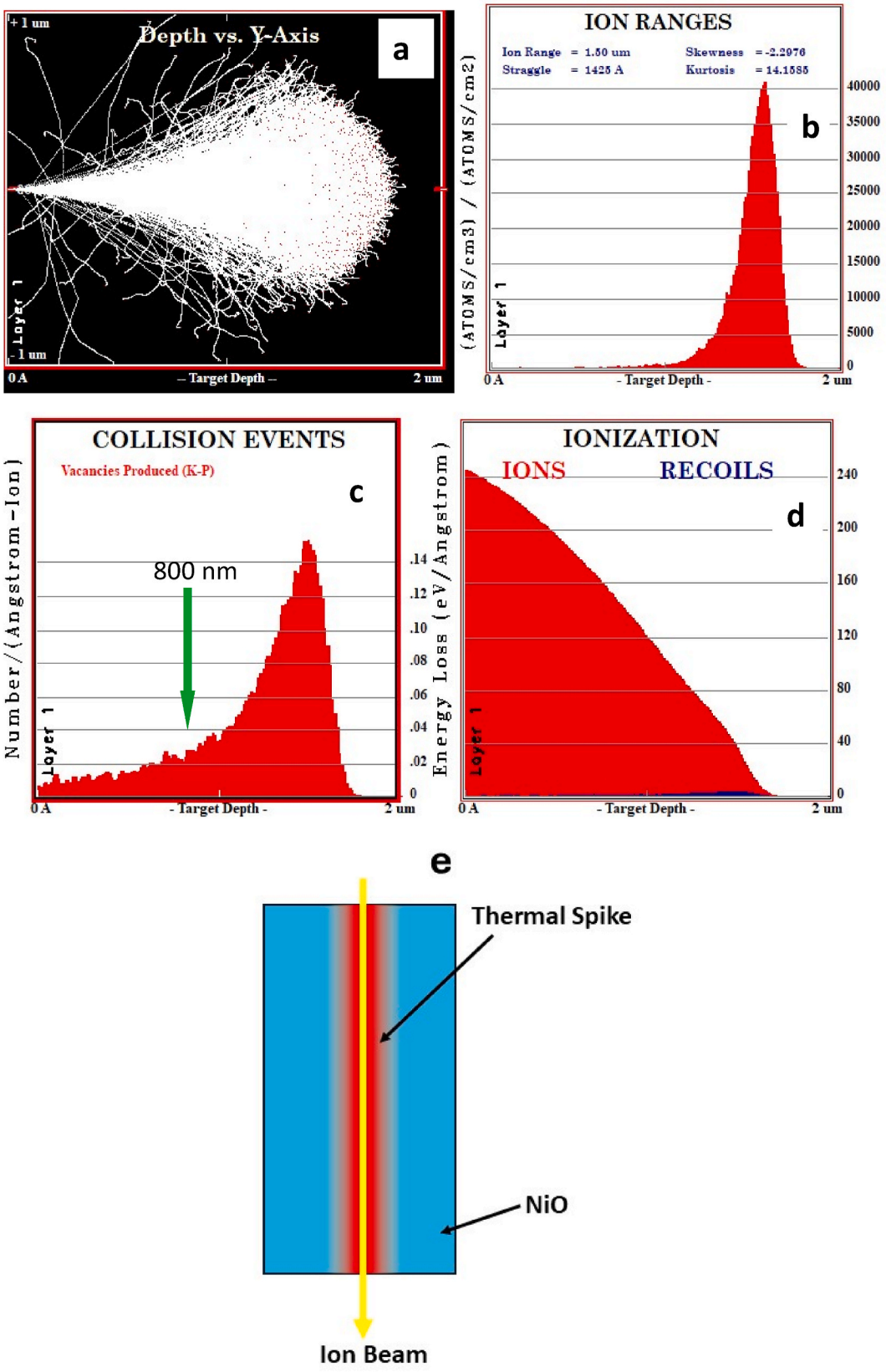

Fig. 2. a) Simulations showing collision cascade in NiO of 2 μm thickness with an incident energy of 2.4 MeV, b) SRIM calculation of the C^{+} ion range within the NiO matrix of 2 μm, c) Simulations showing induced vacancy distribution in NiO matrix, and the arrow shows the thickness of NiO, d) Simulations displaying the ionization level within NiO and e) Energy Deposition along Ion Trajectory in NiO.

2.3. Sample characterization

The crystal structure of all the samples was investigated using X-ray diffraction (XRD) with a Bruker D8 Advance instrument, utilizing Cu Kα radiation (λ = 1.54060 Å). The vibrational modes of the unirradiated and irradiated samples were studied using a Raman spectrometer via Horiba Labram HR Evolution with a laser excitation wavelength of 532 nm. The surface morphology of the samples was performed with a Zeiss Sigma 300 VP high-resolution scanning electron microscope (HRSEM) equipped with an energy dispersive spectroscopy (EDS) accessory for compositional analysis, as well as an atomic force microscope (AFM). Changes in the optical properties of NiO nanostructured thin films were investigated through optical measurements using a Cary 500 UV–Vis–NIR spectrophotometer. The electrical properties were investigated using the Ecopia AMP 55T HMS-5300-HMS 5500 hall measurement system.

3. Results and discussion

3.1. SRIM simulations

SRIM Monte Carlo simulations were performed to simulate the distribution of the incident ions of carbon in the irradiated NiO nanostructured thin films, as well as the radiation damage in terms of the production of vacancies. The penetration depth profiles of C^+ ions as they were irradiated at 2.4 MeV into NiO nanostructured thin films are displayed in Fig. 2. The thickness of NiO nanostructured thin films was 800 nm, and the projected range of 2.4 MeV C^+ ions was calculated to be 1500 nm. This clearly shows that the projected range is greater than the thickness of the NiO nanostructured thin films, which confirms that the

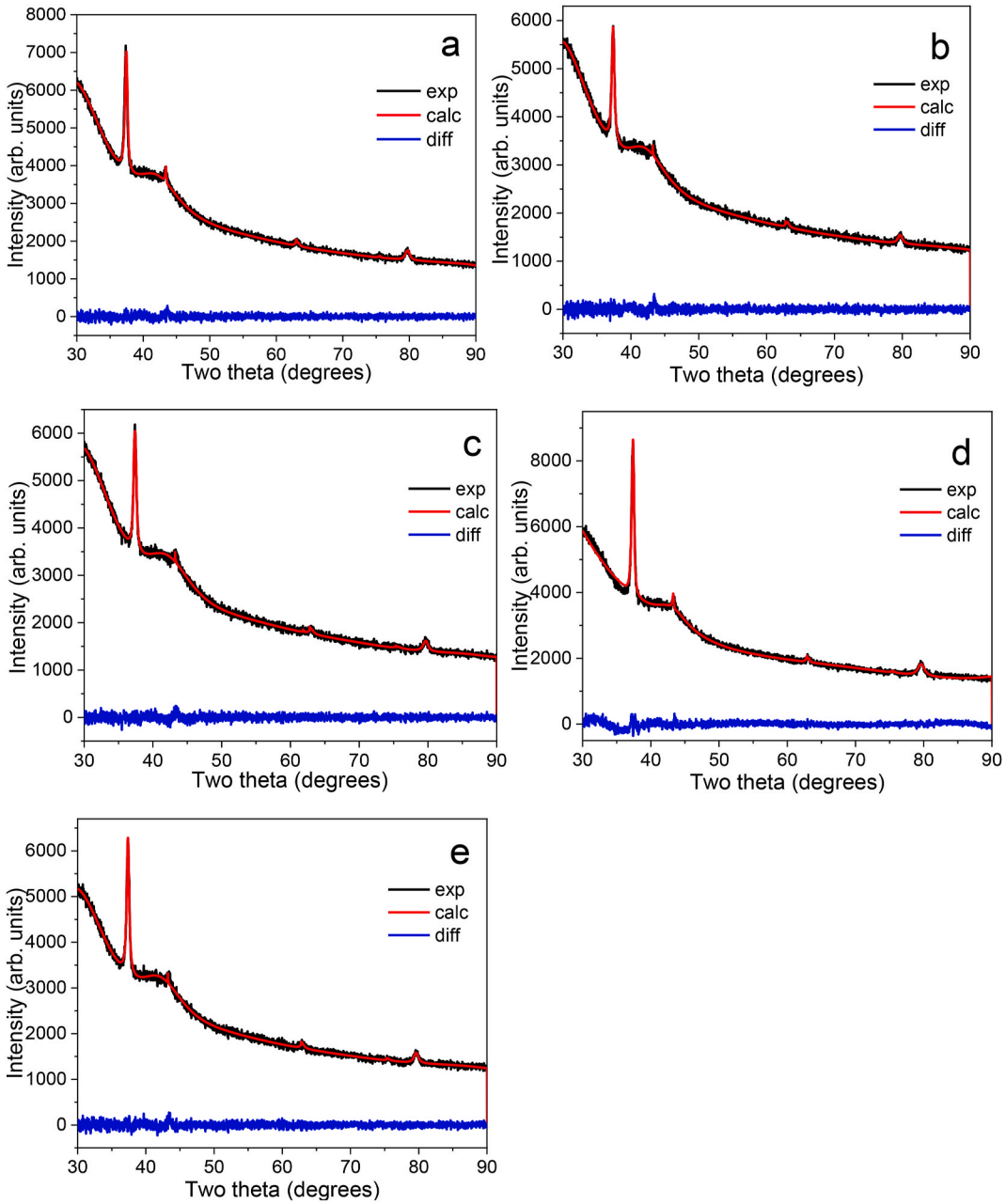

Fig. 3. Rietveld refined XRD patterns showing the experimental (black line) and calculated (red line) for a) pristine NiO, b) C-NiO 2×10^{13} ions/cm^2, c) C-NiO 1×10^{14} ions/cm^2, d) C-NiO 2×10^{14} ions/cm^2, and e) C-NiO 1×10^{15} ions/cm^2. The bottom blue line in each spectrum shows the difference between the refined and the experimental data. (For interpretation of the references to colour in this figure legend, the reader is referred to the Web version of this article.)

C^+ ions traversed the film and stopped in the substrate. The energy loss within the NiO thin films for the incoming C^+ ions is exclusively attributed to electronic stopping due to the electronic excitations and ionization. Specifically, the stopping calculations indicate that the two energy loss mechanisms for 2.4 MeV C^+ ions, nuclear stopping (S_n) and electronic stopping (S_e), correspond to 2.52 eV/Å and 153.20 eV/Å, respectively. The S_e is way much larger than the S_n due to the highly energetic C^+ ions, which interact primarily with the electrons rather than the nuclei on their pathway.

3.2. XRD analysis

The X-ray diffraction (XRD) patterns were used to investigate the impact of C^+ ion irradiation on the structural parameters of NiO nanostructured thin films analysed using Rietveld refinement technique by employing Total pattern analysis (TOPAS). The Rietveld refinement method uses a least-square approach to compare intensities from the structural mode to the Bragg intensities. This is done by considering the structural parameters including profile shape, lattice parameters, atomic coordinates, preferred orientation, and isothermal parameters. The refinement gives exact peak fittings for the typical patterns of pure NiO with minor refinement errors [37]. A Lorentzian function was employed for the refinement. The Rietveld refinement XRD data for the pristine NiO and all irradiated samples are presented in Fig. 3, clearly showing good agreement between the observed and calculated patterns. The refined data have confirmed that all the experimental peaks correspond to the allowed Bragg 2Θ positions for *Fd3 – m* space group. As confirmed by the refinement all samples display a preferred orientation, which is observed at 2Θ angle of about 37.35°, attributed to the (111) face-centered structure of NiO [38,39]. Secondary peaks or impurities were not observed in the XRD spectra, and as expected, no carbon-related diffraction peaks were observed. The radiation damage induced by the impact of C^+ ions in the NiO matrix results in variations in the crystallite size. The (111) peak position, lattice parameter, a, and atomic position as shown in Table 1, were not affected by the C^+ ions. Therefore, the deposited energy was not high enough to result in a notable atomic displacement that would modify the bond lengths and angles in the NiO cubic structure. The results are consistent with the SRIM vacancy production profile shown in Fig. 2c.

The quality of fit for the structure, peak shape, peak position, and background is evaluated using profile R-factors, as displayed in Table 1. The values of R factors obtained are quite small with values less than 3. This justifies a good agreement between the calculated diffraction data and the observed data. Therefore, the refined structural model properly matches the experimental data. Fig. 4 presents the XRD spectra of the unrefined data, and the standard employed during analysis.

Table 1
Rietveld refinement parameters of pristine NiO and C^+ irradiated samples.

Structural Parameters	Pristine NiO	C-NiO 2 × 10^{13}	C-NiO 1 × 10^{14}	C-NiO 2 × 10^{14}	C-NiO 1 × 10^{15}
2Θ (°) (111)	37.3596	37.3615	37.3653	37.3437	37.3553
Lattice constant (Å) a = b = c	4.1823	4.1833	4.1823	4.1820	4.1831
Unit-cell volume (Å^3)	73.1546	73.2072	73.1575	73.1395	73.1974
Density (g/cm^3)	6.782	6.777	6.781	6.783	6.778
GoF	1.07	1.07	1.04	1.10	1.07
R_{wp} (%)	2.11	2.22	2.15	2.20	2.26
R_P (%)	1.64	1.72	1.67	1.70	1.77
R_{exp} (%)	1.98	2.08	2.06	1.99	2.12
Atomic Position	**x**	**y**	**z**		
Ni1	0	0	0		
O1	0.5	0.5	0.5		

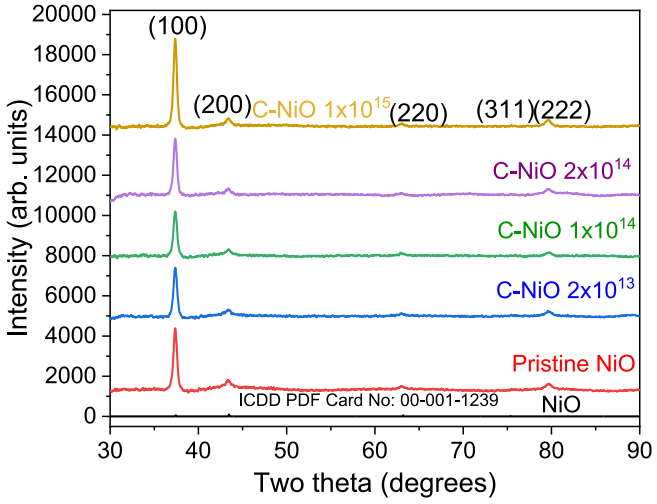

Fig. 4. XRD analysis of pristine NiO, C^+ ion irradiated samples, and XRD pattern for standard NiO, based on card no: 00-001-1239.

The broadening of the XRD peaks was employed in crystallite size analysis. The peak broadening is contributed by various factors such as instrumental effect, strain effect within the crystal lattice, and crystallite size [40]. The crystallite size was determined using the refinement data and the Scherrer equation. The crystallite size calculated using the two methods follows the same trend, but the D of the refinement data are greater than of Scherrer equation. This is attributed to the fact that Rietveld refinement accounts for all instrumental factors and effects of peak broadening [40]. The results are shown in Table 2.

At lower C^+ ion fluences, the samples exhibit peak broadening with a slight reduction in crystallite size and a decrease in peak intensity, which is attributed to the formation of various defects that cause strain and disorder within the host [41]. At higher carbon irradiation (2×10^{14} and 1×10^{15} ions/cm^2), there is a notable rise in crystallite size attributed to the thermal spike model [42,43]. The inelastic energy loss results in the production of a narrow track with highly excited electrons. The energy of these excited electrons spreads via electron-electron interactions until they gain sufficient thermal energy to transfer it to the material's atoms through electron-phonon coupling. This causes the lattice temperature to rise quickly, followed by a very swift cooling phase that lasts only a few picoseconds. The localized thermal spike can result in structural modifications, such as defect formation, the formation of ion tracks, or a recovery process where pre-existing damage regroups [7]. The thermal spike induced within the NiO matrix caused structural alterations by recombining defects, leading to a recovery process that promoted crystalline growth [2]. Fig. 2e shows the thermal spike effect due to electronic stopping within the NiO matrix.

It can be concluded that C^+ ion irradiation favours the crystal growth of NiO at high irradiation fluence. The increase in C^+ ion fluence results in an increase in total energy deposited in the film. This phenomenon echoes findings from previous authors, such as Khalida et al. [44], who noted an increase in crystallite size of polycrystalline tungsten irradiated with C^+ ions of 0.5×10^{15} ions/cm^2. The noted reduction in FWHM and the growth of crystallite size can also be ascribed to the diffusion of the

Table 2
Average crystallite size compiled using Scherrer and Rietveld methods.

Sample	Scherrer (nm)	Refined data (nm)
Pristine NiO	17.28	23.5
C-NiO 2 × 10^{13}	16.95	22.8
C-NiO 1 × 10^{14}	17.08	23.6
C-NiO 2 × 10^{14}	17.95	24.7
C-NiO 1 × 10^{15}	18.18	25.5

host atoms beyond grain boundaries [41]. At higher fluences, the film alleviates strain, resulting in an enhancement of crystallite size. The Scherrer equation (1) was used to determine the crystallite size [45]:

$$D = \frac{k\lambda}{\beta \cos\theta} \quad (1)$$

where k is the Scherrer's constant, 0.9, β is the full width at half maxima (FWHM), and λ is the X-ray wavelength, Θ is the Bragg diffraction angle.

The results reveal that the irradiation caused localized damage without resulting in a complete structural transformation.

3.3. Raman analysis

Raman analysis was also employed to investigate the defect-induced variations in the crystal structure of NiO nanostructured thin films. All samples exhibited three prominent peaks associated with the lattice vibrations of NiO. These typical NiO peaks arise from phonon scattering. The first-order phonon (1P) mode is located at 236 cm^{-1} in all the samples. Additionally, a shoulder peak ascribed to the first-order transverse optical mode (1TO), appears around 365 cm^{-1} for all the samples. Another shoulder band, located around 450 cm^{-1}, is ascribed to the surface optical mode (1SO). The presence of the 1SO mode

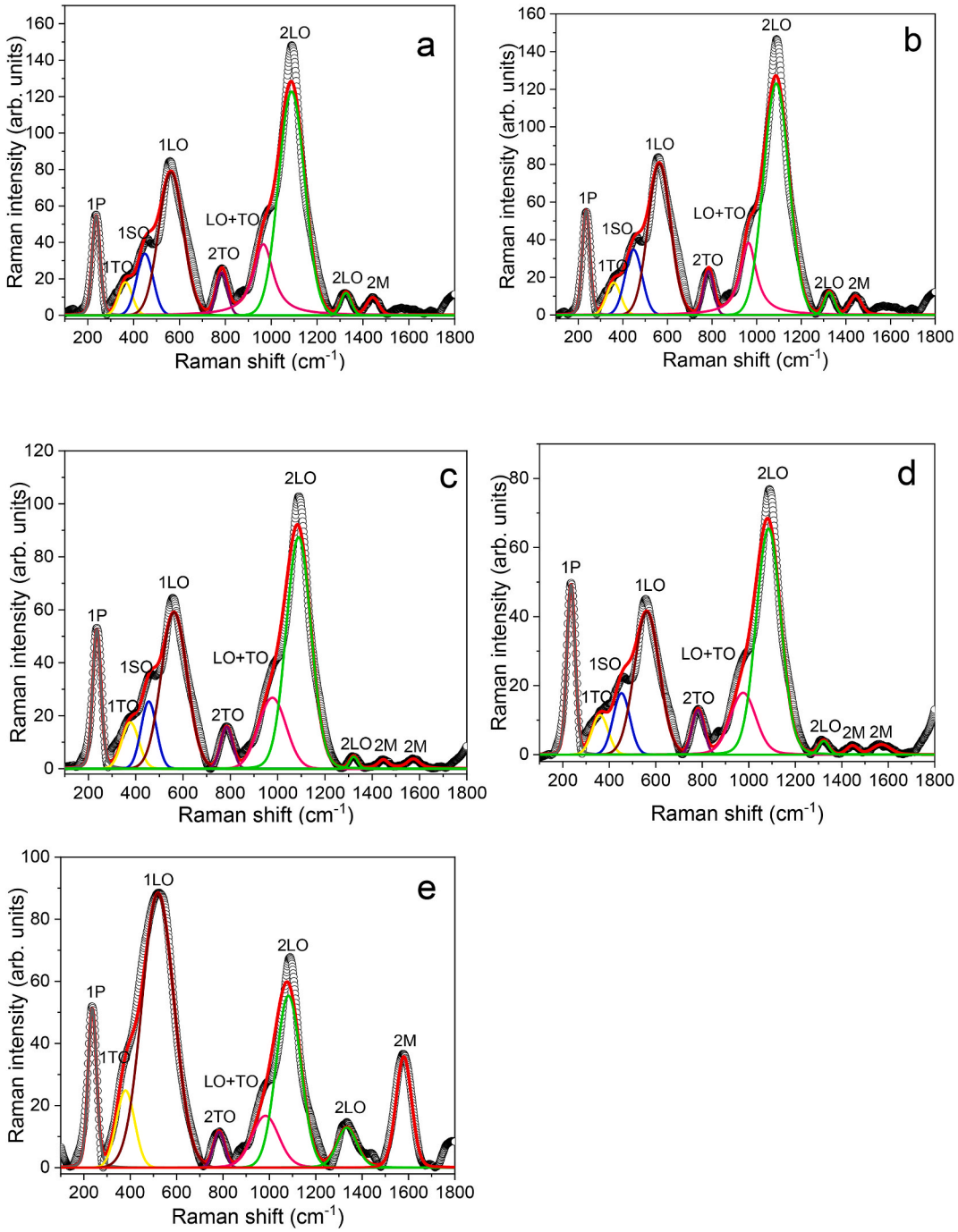

Fig. 5. Deconvoluted Raman spectra using Voight function for a) Pristine NiO b) C-NiO 2×10^{13}, c) C-NiO 1×10^{14}, d) C-NiO 2×10^{14}, e) C-NiO 1×10^{15} ions/cm^2. The colours grey, yellow, blue, wine, purple, pink, green, and red represent the fittings for 1P, 1TO, SO, 1LO, 2TO, LO + TO, 2LO and 2M vibrational modes, respectively. The Voight cumulative fit peak is represented by the red colour. (For interpretation of the references to colour in this figure legend, the reader is referred to the Web version of this article.)

signifies the surface defects in the NiO nanoparticles [46]. However, this band disappears in the sample irradiated with the highest C^+ ion fluence (1×10^{15}) which could be due to its overlap with the 1LO mode, resulting in a different spectral shape compared to the pristine sample. This is clearly revealed by the deconvoluted Raman spectrum. The longitudinal mode (1LO) for pristine NiO is located at 563 cm^{-1}. Alterations to the 1LO mode were observed upon ion beam energy transmission to the NiO matrix. These changes include a decrease in peak intensity and peak width, as well as a shift towards a lower Raman wavenumber associated with the 1LO mode in irradiated samples up to a fluence of 2×10^{14} ions/cm^2. The reduction in the intensity of the 1LO mode after ion bombardment is attributed to electronic excitations and ionization [47]. The presence of the 1LO and 1TO modes is attributed to the nickel vacancies and structural imperfections in the NiO nanoparticles [48,49]. The 1LO Raman peak shifts to 519 cm^{-1} for the sample with the highest C^+ ion fluence, (1×10^{15} ions/cm^2), with a broader peak width observed. An increase in intensity is also observed for the 1LO peak at this fluence, which is ascribed to the increase in electron-phonon coupling effect [50]. The discrepancies in Raman modes are ascribed to distortions and defects within the host lattice induced by highly energetic ions [51]. Additionally, previous authors associate Raman shifts with surface modifications resulting from charge transfer between the host lattice and incident ions [52]. A peak at 784 cm^{-1}, ascribed to the 2TO mode, is present in all samples. The 2LO mode noted at 1089 cm^{-1} for pure NiO, is also observed in all samples, as shown in Fig. 5. The 2LO and 2TO bands represent the stretching modes of NiO [48]. The intensity of the 2LO vibrational mode decreases upon irradiation, and this peak also narrows with increasing carbon ion fluence. The 2LO mode shifts slightly to a lower wavenumber, from 1089 cm^{-1} for pristine NiO to 1082 cm^{-1} at the highest irradiation fluence (1×10^{15} ions/cm^{-2}). This variation in the peak further validates the presence of structural defects within the NiO structure [51]. The two-magnon (2M) mode, observed at 1442 cm^{-1} for pristine NiO, is attributed to the magnetic excitation of NiO nanoparticles [49,53,54].

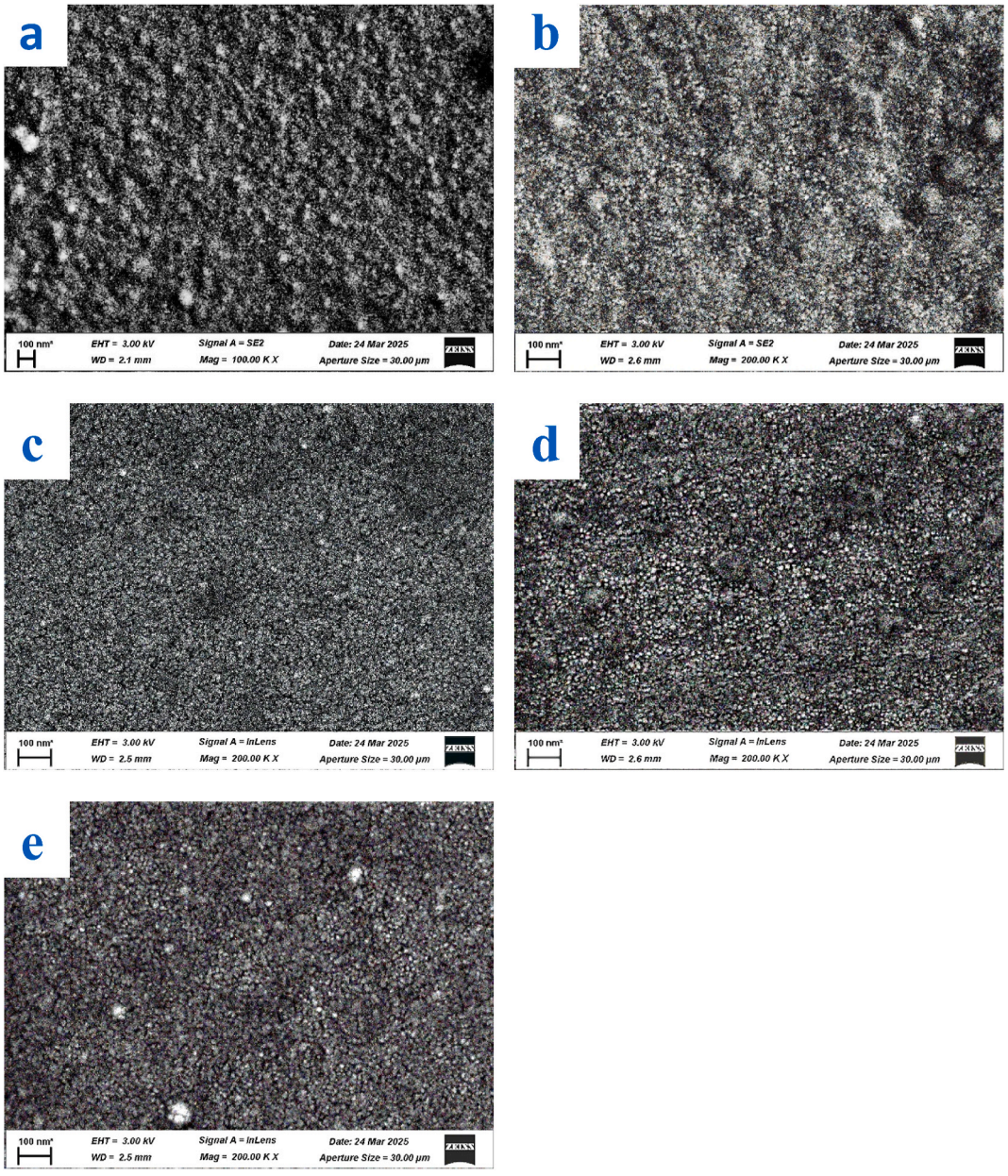

Fig. 6. SEM images of pristine NiO (a), C-NiO 2×10^{13} (b), C-NiO 1×10^{14} (c), C-NiO 2×10^{14}(d), and C-NiO 1×10^{15} (e). Particle size distribution of f) pristine NiO and g) C-NiO 1×10^{15} and EDS analysis of pristine NiO (h), and C-NiO 1×10^{15} (i).

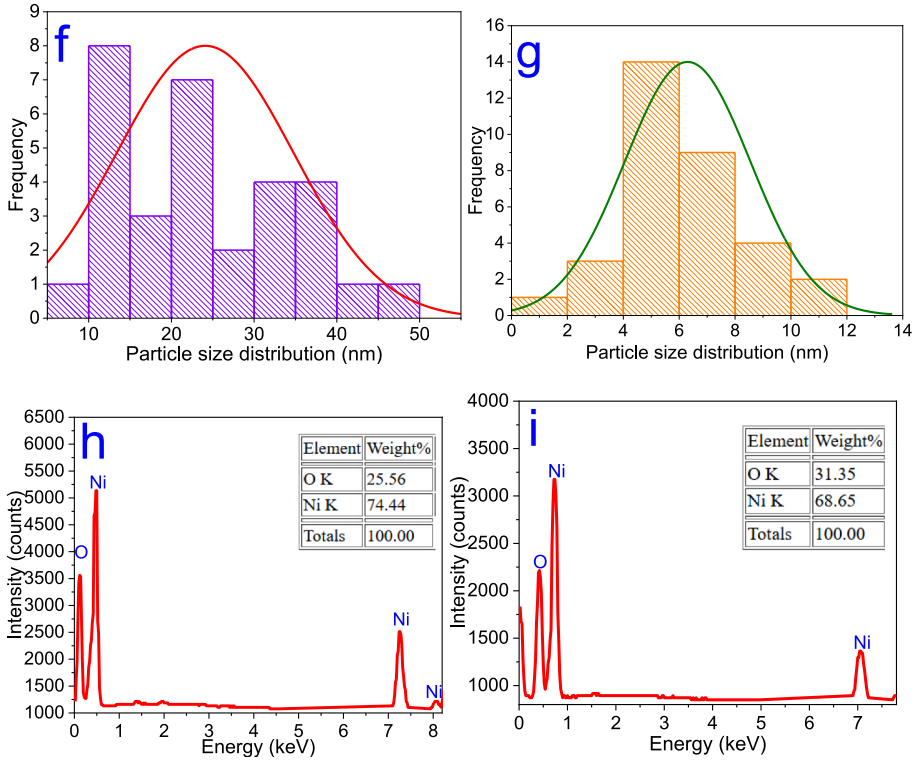

Fig. 6. (*continued*).

Its peak intensity increased during irradiation but diminished at high C^+ ion fluences (2×10^{14} and 1×10^{15} ions/cm^2). Additionally, a second 2M peak emerges at 1574 cm^{-1} for samples irradiated at fluences of 1×10^{14}, 2×10^{14}, and 1×10^{15} ions/cm^2. The emergence of this peak is accompanied by a shift of the 2M band to higher wavenumbers, along with an increase in its intensity at a fluence of 1×10^{15} ions/cm^2. The magnetic behaviour of NiO nanoparticles can be influenced by various factors, including the annealing state and the presence of oxygen ion (O^{2-}) and nickel ion (Ni^{2+}) vacancies [55,56]. Therefore, the variation in the 2M peak verifies that the energy transferred through electronic stopping significantly induces structural modifications at high irradiation fluences.

3.4. SEM analysis

The SEM images of all the samples are displayed in Fig. 6. The

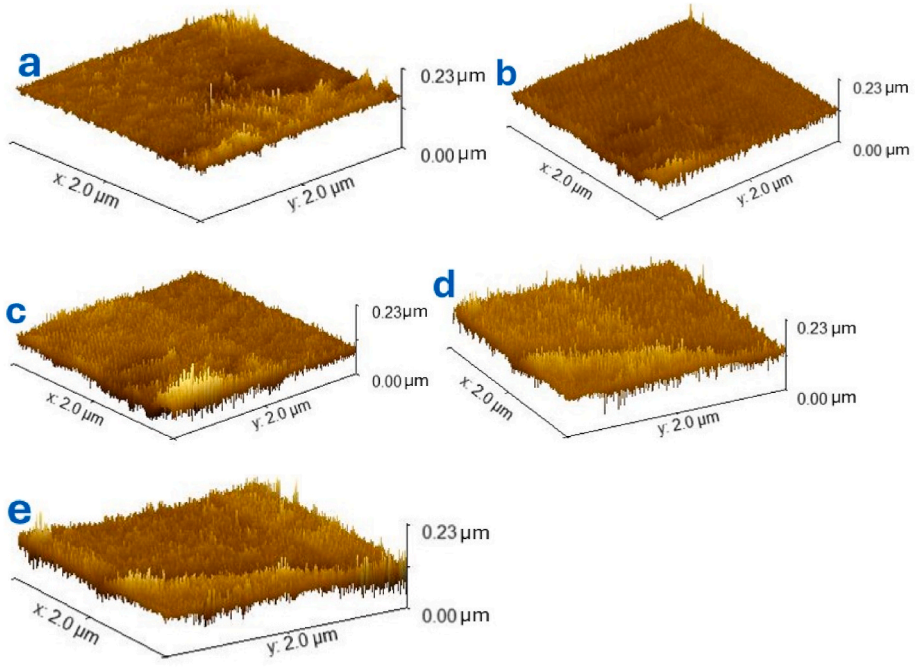

Fig. 7. 3D AFM images of Pristine NiO and C^+ ion irradiated samples.

observed nanoparticles in both pristine and irradiated samples appear granular. All samples show fine particles of different sizes. The pristine NiO exhibited an average particle size of 28 nm. Upon bombardment with a C^+ ion beam, the average particle size was reduced to 8 nm for samples exposed to ion fluences of 2×10^{13}, 1×10^{14}, and 2×10^{14} ions/cm^2. Furthermore, when the ion fluence was increased to 1×10^{15} ions/cm^2, the average particle size further decreased to 6 nm. No cracks or pinholes were observed on the surface of the film. This helps create a homogeneous nucleation and strong adhesion. The particle size distribution graphs for pristine NiO and C-NiO 1×10^{15} ions/cm^2 are shown in Fig. 6f and g, respectively. The results are similar to those reported by Mallick et al. [57], which show a reduction in NiO particle size due to ion irradiation. The elemental composition of pristine NiO thin film and the sample with higher fluence are shown in Fig. 6h and i, respectively. The EDS spectra for all samples displayed peaks corresponding to the Ni and O elements, with no impurity peaks detected, as verified by XRD. Fig. 7 shows the 3D surface topography AFM images of the pristine and C^+ ion irradiated samples. The micrographs reveal finely distributed particles, consistent with the SEM images. As the C^+ ion fluence increases, there is a corresponding increase in the average roughness (R_a) and root mean square roughness ($R_{q)}$, as shown in Table 3. The R_a increases from 7.10 nm for pristine NiO to 14.65 nm at a fluence of 2×10^{14} ions/cm^2. The increase in roughness is attributed to collision cascades that induce surface defects. However, at a higher ion fluence (1×10^{15} ions/cm^2), both Ra and Rq decrease, symbolizing a smoothing effect as a result of accumulated energy.

3.5. UV–Vis analysis

The optical properties of pristine NiO and ion irradiated samples were studied using Ultraviolet–Visible (UV–Vis) spectrophotometer. The transmittance in the visible region for pristine NiO was 56 %, it increased to 62 % for samples that had been bombarded with carbon ions at 1×10^{14} ions/cm^2 and decreased to 47 % at the highest carbon ion fluence. The transmittance of the samples does not display interference fringes due high crystallinity of the samples, which is consistent with previous research [58,59]. This is evident in Fig. 8a. The diminish of the transmittance at higher carbon fluence is ascribed to the higher electron carrier density and induced defects as oxygen vacancies [9,60]. The reduction of the optical transmittance might also be due to the occurrence of scattering at the grain boundaries [61].

The influence of carbon irradiation on the optical properties of NiO was further investigated via determining the absorption and extinction coefficients. The absorption coefficient (α) was calculated using equation (2) [62]:

$$\alpha = \frac{1}{t}.\ln\frac{1}{T} \tag{2}$$

where T is the transmittance and t is the thickness of the film. The extinction coefficient (k) was computed using equation (3) [63] and the results are plotted in Fig. 9a:

Table 3
The roughness parameters of Pristine NiO and C^+ irradiated samples.

Sample	Average roughness (R_a) (nm)	Root mean square roughness (R_q) (nm)
Pristine NiO	7.10	9.66
C-NiO 2×10^{13}	7.75	10.41
C-NiO 1×10^{14}	12.64	16.71
C-NiO 2×10^{14}	14.65	18.90
C-NiO 1×10^{14}	11.91	15.51

$$k = \alpha\lambda/4\pi \tag{3}$$

The absorption coefficient is a measure of how much light a material can collect or trap. High C^+ ion irradiations enhance the absorption property of NiO. The results reveal that there are variations in the absorption and extinction coefficients in the visible region post irradiations. The absorption coefficient is associated with direct band transitions. The Tauc model was used to determine the energy band gap [64–66]:

$$\alpha hv = K\left(hv - E_g\right)^{1/2} \tag{4}$$

where K is a constant expressing the transition probability of the material, h is the Planck's constant, v is the frequency of the photon, and E_g is the energy band gap. The Tauc plots displayed in Fig. 9b were used to determine the optical band gap of the NiO samples. The band gap values were obtained by extrapolating the linear portion of the $(\alpha hv)^2$ against hv plot to the photon energy (hv) axis, where $(\alpha hv)^2 = 0$. The calculated band gap values are presented in Table 4, with the pristine NiO exhibiting a band gap of 3.24 eV, while samples irradiated at 2×10^{13}, 1×10^{14}, 2×10^{14}, and 1×10^{15} ions/cm^2 revealed band gaps of 3.29, 3.39, 3.19, and 2.80 eV, respectively.

The energy band gap of pristine NiO falls within the range of values previously reported [67,68]. There is some disparity in the energy band gaps due to irradiation-induced defects. It has been observed that at lower carbon ion fluence, the energy band gap increases from 3.24 to 3.39 eV at a fluence of 1×10^{14} ions/cm^2. The increase in the band gap can be attributed to the modifications caused by defects and the strain induced by irradiation. The results are similar to those from previous studies by Solanki et al. [4], who reported on the increase in energy band gap for strontium titanate thin films irradiated at the lowest fluence. The increment in the band might also be due to the quantum confinement effect since SEM displays a reduction in particle size after ion irradiation. This is in concurrence with previous research [69] as the variations in the band gap were ascribed to the enhanced quantum size effect. It is worth noting that the band gap of the irradiated NiO films decreases at higher irradiation fluence. The reduction in band gap is due to the development of defect states in the energy band, which also modifies the electronic structure of the target material. Furthermore, the diminishing of the band gap could be due to ionization which results in a high-density of band-tail states [70,71]. It can be concluded that high carbon ion irradiation promotes electron flow since it eases swift photoexcitation of electrons from the conduction band of NiO. One of the merits of this study is that it shows how high C^+ ion fluences can narrow the band gap of NiO, changing its properties. Therefore, it is ideal for consideration in various modern technology applications, including energy storage, transparent conductive oxides (TCOs), sensors, photocatalysis, light-emitting diodes (LEDs), optoelectronics, and photovoltaic cells.

The optical depth penetration (ODP) also known as skin depth was calculated using equation (5):

$$ODP = 1/\alpha \tag{5}$$

It is inversely proportional to the absorption coefficient. During ion irradiation, the skin depth increases and then decreases as the C^+ ion fluence increases as observed in Fig. 10a. The Urbach energy, E_u was used to study the disorder of the pristine and ion irradiated NiO structure. This optical parameter can be computed using the formula [61]:

$$\alpha = \alpha_0 \exp\left(\frac{hv}{E_u}\right) \tag{6}$$

where h and v are as defined in equation (4), α_0 is a constant and E_u is the Urbach energy. Fig. 10b was used to determine the Urbach energy of the samples from the slope of the linear fit of ln α against hv.

The E_u slightly increases from 2.43 to 2.49 eV at a fluence of 2×10^{13}

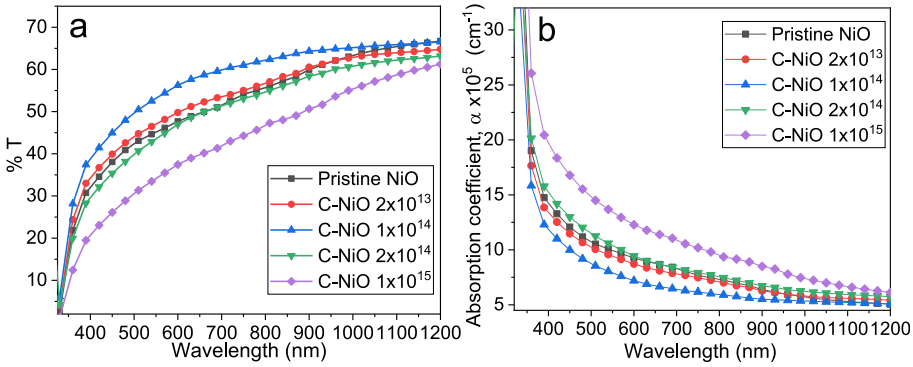

Fig. 8. a) Transmittance spectra and b) the optical absorption coefficient plot of ion-irradiated and pristine NiO thin films.

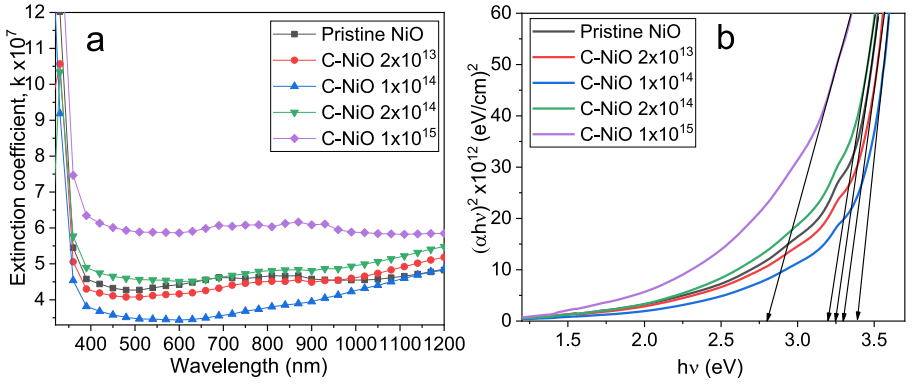

Fig. 9. a) The extinction coefficient and b) Tauc's plot for pristine and ion irradiated NiO samples at different ion fluences.

Table 4
Refractive index using different models, optical energy bandgap, and Urbach energy values of the pristine NiO and carbon irradiated thin films.

Sample	n_o (Moss)	n_o (Herve - Vandamme)	n_o (Ravindra - Gupta)	$E_{g(Tauc)}$ (eV)	*Eu* (eV)
Pristine NiO	2.33	2.20	2.08	3.24	2.43
C-NiO 2 × 10^{13}	2.32	2.19	2.04	3.29	2.49
C-NiO 1 × 10^{14}	2.30	2.16	1.98	3.39	2.23
C-NiO 2 × 10^{14}	2.33	2.21	2.11	3.19	2.21
C-NiO 1 × 10^{15}	2.41	2.32	2.35	2.80	2.19

ions/cm^2. The increase in E_u validates the enhancement of disorders and more defects in the NiO structure. However, at a high C^+ ion fluence of 1 × 10^{15} ions/cm^2, the E_u decreases to 2.19 eV. The decrease in E_u means the reduction in the generated defects due to the recrystallization of the samples as observed from XRD.

The refractive index (n) is an important aspect for determining whether materials are suitable for optoelectronic devices. In this study, the static refractive index (n_o) was evaluated using different models to gain a comprehensive understanding of NiO's optical behaviour for its potential applications in advanced technologies. Since the optical refractive index is very important macroscopic parameter, efforts have been made to develop simple relations that connect the optical refractive index to the energy band gap [72]. Different models, including Moss, Herve-Vandamme and Ravindra-Gupta which correlate the optical refractive index of the material to its plasmon energy band gap have been proposed [72–74]. All these models demonstrated high accuracy in

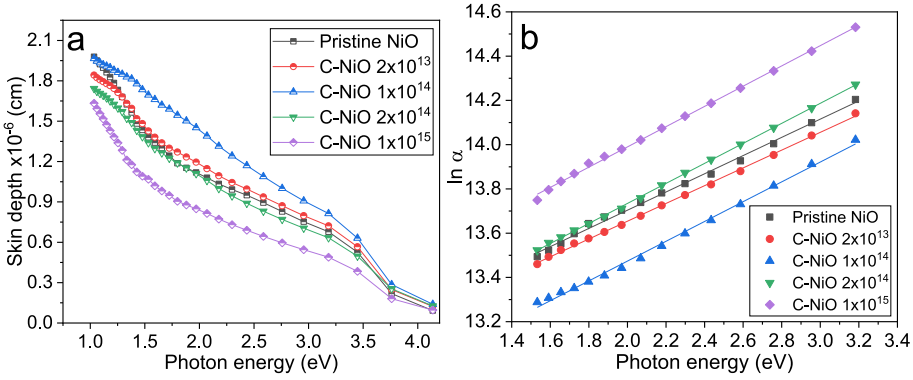

Fig. 10. a) Skin depth and b) Urbach energy extrapolations for pristine NiO and irradiated samples at various ion fluences.

computing the optical refractive index. Table 4 shows the computed static refractive index using these models and illustrates how it varies with ion irradiation.

The Moss relation [75] describes the static/optical refractive index (n_o) as a function of the absorption edge and establishes a direct relationship between E_g and n_o:

$$n_o = \left(\frac{95}{E_g}\right)^{1/4} \tag{7}$$

The Herve-Vandamme [66] equation can be perfectly applied to many optoelectronic materials:

$$n_o = \sqrt{1 + \left(\frac{K}{E_g + B}\right)^2} \tag{8}$$

where K is 13.16 eV which is the hydrogen ionisation energy and B is a constant, 3.47 eV. The refractive index was also computed using a third model, the Ravindra equation [66]:

$$n_o = 4.084 - 0.62E_g \tag{9}$$

The computed static refractive index using all three models follows the same trend both before and after irradiation. As anticipated, there are variations in the refractive index after irradiation due to changes in the electronic structure of the NiO caused by atomic defects from the irradiation. The electronic excitation affects the material's density, which in turn influences the refractive index, leading to the observed variations post-irradiation. The static refractive index values obtained using the Moss equation display the highest values compared to the other two models. Among the samples, the one irradiated with the highest C^+ ion fluence exhibits the highest refractive index, making it more desirable for optoelectronic devices.

It is crucial to determine the dielectric behaviour of solids especially if we are considering exploring them for electronic devices. Equation (10) was used to determine the high-frequency lattice dielectric constant (ε_∞) [76]:

$$\varepsilon_\infty = n_o^2 \tag{10}$$

where n is the refractive index. The static dielectric constant (ε_o) of the films was computed using a formula that gives the dependence of ε_o on the energy band gap for semiconductor compounds [77]:

$$\varepsilon_o = 18.52 - 3.08E_g \tag{11}$$

The values of ε_∞ and ε_o are presented in Table 5. The high-frequency lattice dielectric constants for all the models follow the same trend as the static refractive index, as they depend on (n). The static dielectric constant decreases at lower C^+ ion fluences (2×10^{13} and 1×10^{14} ions/cm^2) and increases at higher C^+ ion fluences (2×10^{14} and 1×10^{15} ions/cm^2).

3.6. Electrical properties

The electrical measurements of all the samples were studied at room temperature and the parameters are displayed in Table 6. Fig. 11 illustrates changes in resistivity and mobility upon irradiation. The resistivity was used to determine conductivity. The defects in the NiO atoms contributed to the increase in resistivity from 0.102 to 0.124 Ωcm at low C^+ ion fluence. This increase is attributed to the dispersion of charge carriers, which resulted in decreased mobility due to a limited number of free carriers available for conduction.

The increase in resistivity is also contributed by the nickel vacancies and oxygen vacancies created during irradiations [78]. The resistivity then decreases from 0.124 Ωcm at a fluence of 1×10^{14} to 0.0787 Ωcm at 1×10^{15} ions/cm^2. This observation is related to the surge in crystallite size for the sample irradiated with the highest carbon fluence, as obtained from XRD. The enhanced crystallinity leads to fewer grain boundaries while reducing impurity scattering, which in turn improves the charge carriers' pathways [79,80]. This positively impacts the movement of holes, resulting in increased carrier mobility and conductivity.

Furthermore, the sample irradiated at 1×10^{15} ions/cm^2 has a low band gap as already stated, hence the electrons in the valence band acquire enough energy to migrate to the conduction band. Therefore, it is worth noting that high C^+ ion irradiation improves the conductivity and electron mobility of NiO. The relationship between conductivity and resistivity can be explained using the following relation:

$$\sigma = 1/\rho \tag{12}$$

where σ is the specific conductivity and ρ symbolise the resistivity. The resistivity is inversely proportional to conductivity.

4. Conclusion

This study has investigated the effects of 2.4 MeV C^+ ion irradiation on NiO nanostructured thin films at various fluences. C^+ ion irradiation led to changes in microstructural, optical, and electrical properties of NiO nanostructured thin films. Rietveld refinement was used to study the microstructural evolution of NiO using XRD data. The structural parameters were accurately determined as the refined model exhibited an excellent fit with the experimental data. The irradiated samples revealed variations in crystallite size due to the electronic excitation and ionization induced by the 2.4 MeV C^+ ions. High irradiation fluence increased the crystallite size of NiO. The lattice parameters, and peak positions remained unchanged showing that the irradiation did not induce a complete structural modification. Alterations in Raman modes were observed post-irradiation. The 2LO vibrational mode diminished upon irradiation, attributed to the presence of structural defects within the NiO structure. The surface morphology revealed a reduction in particle size and an increase in average roughness due to C^+ ion irradiation. No impurities were detected, as confirmed by EDS. There was substantial variation in the optical band gap after irradiation. Carbon ion irradiation improved the conductivity and mobility of NiO and enhanced the charge carrier path at higher irradiation fluence. The results demonstrate an alteration in the material's behaviour. Therefore, it can be concluded that changes in the NiO matrix after 2.4 MeV C^+ ion irradiation occur through two competing processes: the damaging and

Table 5
Lattice dielectric constants calculated using different models for pristine NiO and carbon-irradiated thin films.

Sample	ε_o	Moss ε_∞	Herve - Vandamme ε_∞	Ravindra - Gupta ε_∞
Pristine NiO	8.54	5.43	4.84	4.33
C-NiO 2×10^{13}	8.39	5.38	4.80	4.16
C-NiO 1×10^{14}	8.08	5.29	4.67	3.92
C-NiO 2×10^{14}	8.69	5.43	4.88	4.45
C-NiO 1×10^{15}	9.90	5.80	5.38	5.52

Table 6
Electrical properties of pristine and carbon ion irradiated NiO samples.

SAMPLE	RESISTIVITY, ρ (Ωcm)	CONDUCTIVITY, σ (1/Ωcm)	MOBILITY (cm^2/Vs)
Pristine NiO	0.1020	9.83	0.514
C-NiO 2×10^{13}	0.1220	8.21	0.165
C-NiO 1×10^{14}	0.1240	8.07	0.098
C-NiO 2×10^{14}	0.0890	11.30	2.990
C-NiO 1×10^{15}	0.0790	12.70	3.220

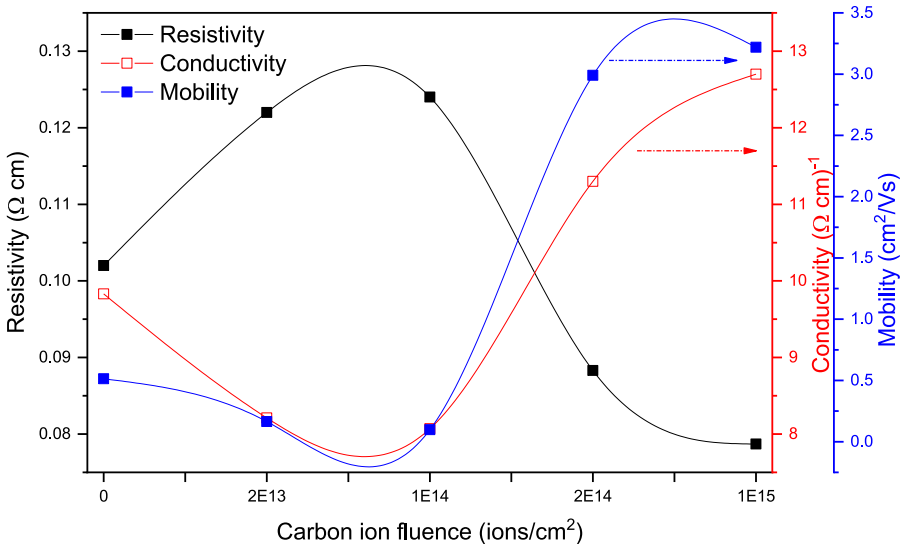

Fig. 11. Electrical measurements of NiO as they vary with C^+ ion irradiation fluences.

thermal spike mechanisms. The thermal spike model dominates at higher C^+ ion fluence, while the damaging effect prevails at lower C^+ ion fluence. In conclusion, the electronic energy loss induced by C^+ ion irradiation in NiO caused significant optical and electronic variations through lattice distortions, ionization, track formation, and localized heating. Carbon ion-irradiated NiO samples would be ideal for various applications, such as transparent conductors, sensors, and different electronic devices. In addition, NiO irradiated at a lower C^+ ion fluence would be ideal for use as a nuclear reactor sensor due to its increased band gap.

CRediT authorship contribution statement

Dineo P. Sebuso: Writing – review & editing, Writing – original draft, Visualization, Software, Resources, Methodology, Investigation, Formal analysis, Data curation, Conceptualization. **Cosmas Muiva:** Writing – review & editing, Validation, Supervision, Resources, Project administration, Funding acquisition, Conceptualization. **Othmane Mouane:** Writing – review & editing, Formal analysis, Data curation. **Rudolph M. Erasmus:** Writing – review & editing, Resources, Data curation. **Morgan Madhuku:** Writing – review & editing, Resources, Project administration, Data curation. **Elias Sideras-Haddad:** Writing – review & editing, Validation, Supervision, Software, Resources, Project administration, Funding acquisition, Conceptualization.

Declaration of competing interest

The authors declare that they have no known competing financial interests or personal relationships that could have appeared to influence the work reported in this paper.

Acknowledgements

This work was supported by funding from the International Atomic Energy Agency (IAEA) through the Botswana national project (funding number FS-BOT1001-2105937, 2023), which the authors deeply appreciate for its crucial role in the project's success. The authors also extend their gratitude to the University of the Witwatersrand, Botswana International University of Science and Technology (BIUST), and iThemba LABS for providing access to research facilities and equipment.

References

[1] B. Bari, S. Honey, M. Madhuku, I. Ahmad, R. Khan, A. Muhammad, K. Alamgir, S. Naseem, M. Maaza, MeV carbon ion irradiation-induced changes in the electrical conductivity of silver nanowire networks, Curr. Appl. Phys. 15 (2015) 642–647, https://doi.org/10.1016/j.cap.2015.02.023.

[2] B. Oryema, E. Jurua, I.G. Madiba, I. Ahmad, S.O. Aisida, F.I. Ezema, M. Maaza, Effects of 7 MeV proton irradiation on microstructural, morphological, optical, and electrical properties of fluorine-doped tin oxide thin films, J. Surf. Interface 28 (2022) 101693, https://doi.org/10.1016/j.surfin.2021.101693.

[3] S. Ahmad, S. Bashir, D. Yousaf, M.A. Ali, Modification in Cu-Zn alloy properties by 2 MeV Ni^+ ions irradiation, J. Mater. Sci. Appl. 9 (2018) 330–344, https://doi.org/10.4236/msa.2018.93022.

[4] A. Solanki, J. Shrivastava, S. Upadhyay, V. Sharma, P. Sharma, P. Kumar, P. Kumar, K. Gaskell, V.R. Satsangi, R. Shrivastav, S. Dass, Irradiation-induced modifications and PEC response-A case study of $SrTiO_3$ thin films irradiated by 120 MeV Ag^{9+} ions, Int. J. Hydrogen Energy 36 (2011) 5236–5245, https://doi.org/10.1016/j.ijhydene.2011.01.149.

[5] F. Chandoul, H. Moussa, K. Jouini, A. Boukhachem, F. Hosni, M.S. Fayache, R. Schneider, Investigation of the properties of nanostructured nickel oxide NiO thin films irradiated at different γ-doses, J. Mater. Sci. Mater. Electron. 30 (2019) 348–358, https://doi.org/10.1007/s10854-018-0299-z.

[6] M.C. Ridgway, R. Giulian, D.J. Sprouster, P. Kluth, L.L. Araújo, D.J. Llewellyn, A. P. Byrne, F. Kremer, P.F. Fichtner, G. Rizza, H. Amekura, Role of thermodynamics in the shape transformation of embedded metal nanoparticles induced by swift heavy-ion irradiation, Phys. Rev. Lett. 109 (2011) 095505, https://doi.org/10.1103/physrevlett.106.095505.

[7] W.J. Weber, D.M. Duffy, L. Thomé, Y. Zhang, The role of electronic energy loss in ion beam modification of materials, Curr. Opin. Solid State Mater. Sci. 19 (2015) 1–11, https://doi.org/10.1016/j.cossms.2014.09.003.

[8] Y. Zhang, W.J. Weber, Ion irradiation and modification: the role of coupled electronic and nuclear energy dissipation and subsequent nonequilibrium processes in materials, Appl. Phys. Rev. 7 (2020) 041307, https://doi.org/10.1063/5.0027462.

[9] S.K. Singh, R. Singhal, R. Vishnoi, V.V.S. Kumar, P.K. Kulariya, Swift heavy ion induced optical and structural modifications in RF sputtered nanocrystalline ZnO thin film, Indian J. Phys. 91 (2017) 547–554, https://doi.org/10.1007/s12648-016-0950-6.

[10] R. Neumann, Science and technology on the nanoscale with swift heavy ions in matter, Nucl. Instrum. Methods Phys. Res., Sect. B 314 (2013) 4–10, https://doi.org/10.1016/j.nimb.2013.04.035.

[11] J.F. Ziegler, M.D. Ziegler, J.P. Biersack, Srim – the stopping and range of ions in matter (2010), Nucl. Instrum. Methods Phys. Res., Sect. B 268 (2010) 1818–1823, https://doi.org/10.1016/j.nimb.2010.02.091.

[12] B. Xia, T. Wang, X. Jiang, J. Li, T. Zhang, P. Xi, D. Gao, D. Xue, N^+ -ion irradiation engineering towards the efficient oxygen evolution reaction on NiO nanosheet arrays, J. Mater. Chem. A (2019) 4729–4733, https://doi.org/10.1039/C9TA00023B.

[13] N. Tripathi, A. Tripathi, R.K. Pandey, V. Bhushan, V. Sharma, Engineering NiO thin film properties using Ag^{9+} ion irradiation at various fluences, ECS J. Solid State Sci. Technol. 1 (2024) 013009, https://doi.org/10.1149/2162-8777/ad1b73.

[14] D. Li, G. Wei, Z. Xing, T. Jiang, Z. Wang, S. Wu, L. Huang, Y. Liu, H. Wu, C. Jiang, F. Ren, Sulfate anchored on the defective NiO by ion irradiation realizes enhanced oxygen evolution reaction, Chem. Eng. J. 485 (2024) 149890, https://doi.org/10.1016/j.cej.2024.149890.

[15] S. Bhakta, P.K. Sahoo, Tuning magnetocrystalline anisotropy by Au ion induced defects in NiO thin films, J. Alloys Compd. 984 (2024) 173844, https://doi.org/10.1016/j.jallcom.2024.173844.

[16] D.K. Mishra, J. Mohapatra, B. Mahato, P. Kumar, A. Mitra, S.K. Singh, D. Kanjilal, Effect of 1.2 MeV argon ions irradiation on magnetic properties of ZnO, Appl. Surf. Sci. 282 (2013) 954–959, https://doi.org/10.1016/j.apsusc.2013.06.098.

[17] T. Li, W. Gao, G. Zhi, S. Zhai, J. Xu, L. Zhang, W. Hu, B. Song, S. Xu, M. Zhou, I2DM: a Monte Carlo framework for ion irradiation on two-dimensional material, Comput. Phys. Commun. 308 (2025) 109445, https://doi.org/10.1016/j.cpc.2024.109445.

[18] S. Ma, S. Ma, G. Ran, Ion beam irradiation techniques: enabling the synthesis, modification and enhancement catalytic applications in nanostructured materials, Mater. Today Chem. 43 (2025) 102529, https://doi.org/10.1016/j.mtchem.2025.102529.

[19] D. Fatto'Offidani, E. Martinez, E.A. Marquis, On the analysis of radiation-induced segregation at ion-irradiated grain boundaries, J. Nucl. Mater. 605 (2025) 155533, https://doi.org/10.1016/j.jnucmat.2024.155533.

[20] A.S. Arico, P. Bruce, B. Scrosati, J.M. Tarascon, W. Van Schalkwijk, Nanostructured materials for advanced energy conversion and storage devices, Nat. Mater. 4 (2005) 366–377, https://doi.org/10.1038/nmat1368.

[21] R. Sharmaa, A.D. Acharya, S.B. Shrivastava, T. Shripathi, V. Ganesan, Preparation and characterization of transparent NiO thin films deposited by spray pyrolysis technique, Optik 125 (2014) 6751–6756, https://doi.org/10.1016/j.ijleo.2014.07.104.

[22] R. Romero, F. Martin, J.R. Ramos-Barrado, D. Leinen, Synthesis and characterization of nanostructured nickel oxide thin films prepared with chemical spray pyrolysis, Thin Solid Films 518 (2010) 4499–4502, https://doi.org/10.1016/j.tsf.2009.12.016.

[23] J.R. Manders, S.W. Tsang, M.J. Hartel, T.H. Lai, S. Chen, C.M. Amb, J.R. Reynold, F. So, Solution-processed nickel oxide hole transport layers in high efficiency polymer photovoltaic cells, Adv. Funct. Mater. 23 (2013) 2993–3001, https://doi.org/10.1002/adfm.201202269.

[24] B. Karthikeyan, S. Hariharan, R.V. Mangalaraja, T. Pandiyarajan, R. Udayabhaskar, P. Sreekanth, Studies on NiO-PVA composite films for opto-electronics and optical limiters, IEEE Photon. Technol. Lett. 30 (2018) 1539–1542, https://doi.org/10.1109/LPT.2018.2859042.

[25] S. Baierl, J.H. Mentink, M. Hohenleutner, L. Braun, T.M. Do, C. Lange, A. Sell, M. Fiebig, G. Woltersdorf, T. Kampfrath, R. Huber, Terahertz-driven nonlinear spin response of antiferromagnetic nickel oxide, Phys. Rev. Lett. 117 (2016) 197201, https://doi.org/10.1103/PhysRevLett.117.197201.

[26] Z. Cheng, R. Fan, J. Liao, G. Yuan, X. Wu, W. Pi, W. Zou, X. Ma, M. Wang, Sensing properties and mechanism of gas sensors based on room-temperature solution processed NiO-Niv nanoparticles, Cryst. Growth Des. 24 (2024) 2900–2908, https://doi.org/10.1021/acs.cgd.4c00006.

[27] X. Wang, X. Li, X. Sun, F. Li, Q. Liu, Q. Wang, D. He, Nanostructured NiO electrode for high rate Li-ion batteries, J. Mater. Chem. 21 (2011) 3571–3573, https://doi.org/10.1039/C0JM04356G.

[28] Y. Abdelbaki, A. de Arriba, R. Issaad, R. Sánchez-Tovar, B. Solsona, J.M. Nieto, Optimization of the performance of bulk NiO catalyst in the oxidative dehydrogenation of ethane by tuning the synthesis parameters, Fuel Process. Technol. 229 (2022) 107182, https://doi.org/10.1016/j.fuproc.2022.107182.

[29] S.J. Mezher, M.O. Dawood, A.A. Beddai, M.K. Mejbel, NiO nanostructure by RF sputtering for gas sensing applications, Mater. Technol. 35 (2020) 60–68, https://doi.org/10.1080/10667857.2019.1653595.

[30] A. Diha, S. Benramache, B. Banhaoua, Transparent nanostructured Co doped NiO thin films deposited by sol–gel technique, Optik 172 (2018) 832–839, https://doi.org/10.1016/j.ijleo.2018.07.062.

[31] B. Sasi, K.G. Gopchandran, Preparation and characterization of nanostructured NiO thin films by reactive-pulsed laser ablation technique, Sol. Energy Mater. Sol. Cells 91 (2007) 1505–1509, https://doi.org/10.1016/j.solmat.2007.04.019.

[32] B.R. Cruz-Ortiz, M.A. Garcia-Lobato, E.R. Larios-Durán, E.M. Múzquiz-Ramos, J. C. Ballesteros-Pacheco, Potentiostatic electrodeposition of nanostructured NiO thin films for their application as electrocatalyst, J. Electroanal. Chem. 772 (2016) 38–45, https://doi.org/10.1016/j.jelechem.2016.04.020.

[33] M.S. Kong, M.S. Park, S.Y. Bae, Post-growth annealing effect of Li-doped NiO thin films grown by mist chemical vapor deposition, Mater. Sci. Eng., B 310 (2024) 117736, https://doi.org/10.1016/j.mseb.2024.117736.

[34] A. Qasem, S. Alraddadi, E. Al-Amery, H.A. Alrafai, E.R. Shaaban, Remarkable effects of laser irradiation in adjusting the structural, morphological, and optical properties of spray pyrolysis-synthesized NiO nanostructured films for optoelectronic applications, Opt Laser. Technol. 164 (2023) 109488, https://doi.org/10.1016/j.optlastec.2023.109488.

[35] B. Brioual, A. El-Habib, Z. Rossi, A. Aouni, M. Addou, M. Diani, R.F. Allah, M. Jbilou, Effect of zirconium doping on structural, optical, and electrochemical properties of NiO thin films: electrochromic application, Next Mater. 6 (2025) 100314, https://doi.org/10.1016/j.nxmate.2024.100314.

[36] C. Muiva, D.P. Sebuso, E. Muchuweni, Microstructural and optical properties of nanostructured al/Ag co-doped ZnO thin films ($Ag_xAl_{0.03}ZnO_{0.97-x}$) by spray pyrolysis for optoelectronic applications, Phys. B: Condens. Mater 690 (2024) 416206, https://doi.org/10.1016/j.physb.2024.416206.

[37] G. Rathika, R. Jagadeeswari, T. Sathiyapriya, P. Selvakumar, Surface and quantum chemical parameters of nickel oxide nanostructures suited for ultraviolet-assisted cationic dye degradation, Kuwait J. Sci. 51 (2) (2024) 100200, https://doi.org/10.1016/j.kjs.2024.100200.

[38] Z. Chen, T. Dedova, I.O. Acik, M. Danilson, M. Krunks, Nickel oxide films by chemical spray: effect of deposition temperature and solvent type on structural, optical, and surface properties, Appl. Surf. Sci. 548 (2021) 149118, https://doi.org/10.1016/j.apsusc.2021.149118.

[39] N.V. Srinivasa, K. Haunsbhavi, N. Srinatha, H.M. Mahesh, B. Angadi, Preparation and characterization of Sn doped NiO thin films by sol–gel spin coating technique, Mater. Today Proc. 92 (2023) 1431–1437, https://doi.org/10.1016/j.matpr.2023.05.597.

[40] L. Kumar, P. Kumar, A. Narayan, M. Kar, Rietveld analysis of XRD patterns of different sizes of nanocrystalline cobalt ferrite, Int. Nano Lett. 3 (2013) 1–12, https://doi.org/10.1186/2228-5326-3-8.

[41] S. Ahmad, S. Bashir, N. Ali, Umm-i-Kalsoom, D. Yousaf, Faizan-ul-Haq, A. Naeem, R. Ahmad, M. Khlaeeq-ur-Rahman, Effect of ion irradiation on the surface, structural and mechanical properties of brass, Nucl. Instrum. Methods Phys. Res., Sect. B 325 (2014) 5–10, https://doi.org/10.1016/j.nimb.2014.01.023.

[42] M. Toulemonde, E. Paumier, C. Dufour, Thermal spike model in the electronic stopping power regime, Radiat. Eff. Defect Solid 126 (1993) 201–206, https://doi.org/10.1080/10420159308219709.

[43] M.F. Khan, K. Siraj, A. Sattar, H. Faiz, A. Usman, A. Raisanen, Modification of structural and electrical properties of ZnO thin films by Ni^{2+} ions irradiation, Dig. J. Nanomater. Biostruct. 12 (2017) 689.

[44] M.L. Khalida, A. Nawaz, B. Islam, F. Aslam, W. Mao, C. Lu, Effect of carbon ion irradiation on the structural, mechanical and electrical properties of polycrystalline tungsten, Mater. Res. Express 6 (2019) 066551, https://doi.org/10.1088/2053-1591/ab087f.

[45] D.P. Sebuso, A.T. Kuvarega, K. Lefatshe, C.K. King'ondu, N. Numan, M. Maaza, C. M. Muiva, Green synthesis of multilayer Graphene/ZnO nanocomposite for photocatalytic application, J. Alloys Compd. 900 (2022) 163526, https://doi.org/10.1016/j.jallcom.2021.163526.

[46] A. Sunny, K. Balasubramanian, Plasmon induced enhancement of surface phonon and magnon properties of NiO, Phys. Chem. Chem. Phys. 22 (2020) 22815–22822, https://doi.org/10.1039/D0CP03720F.

[47] Y. Zhang, C. Silva, T.G. Lach, M.A. Tunes, Y. Zhou, L. Nuckols, W.A. Boldman, P. D. Rack, S.E. Donnelly, L. Jiang, L. Wang, W.J. Weber, Role of electronic energy loss on defect production and interface stability: comparison between ceramic materials and high-entropy alloys, Curr. Opin. Solid State Mater. Sci. 26 (2022) 101001, https://doi.org/10.1016/j.cossms.2022.101001.

[48] K.N. Patel, M.P. Deshpande, V.P. Gujarati, S. Pandya, V. Sathe, S.H. Chaki, Structural and optical analysis of Fe doped NiO nanoparticles synthesized by chemical precipitation route, Mater. Res. Bull. 106 (2018) 187–196, https://doi.org/10.1016/j.materresbull.2018.06.003.

[49] A. Khan, M. Saad, T. Kamal, F. Rahman, Structural, morphological, optical and UV-light driven enhanced photocatalytic properties of Fe-doped NiO nanoparticles, Mater. Chem. Phys. 305 (2023) 127923, https://doi.org/10.1016/j.matchemphys.2023.127923.

[50] W. Wang, Z. Mao, Y. Ren, F. Meng, W. Shi, B. Zhao, Operando Raman spectroscopic evidence of electron–phonon interactions in NiO/TiO2 pn junction photodetectors, Chem. Commun. 57 (2021) 12333–12336, https://doi.org/10.1039/D1CC05303E.

[51] A. Tripathi, V. Bhushan, V. Sharma, 60 MeV Si ion beam irradiation induced modifications in the structural and optical properties of Li doped NiO thin films, Mater. Today Proc. 83 (2023) 19–23, https://doi.org/10.1016/j.matpr.2023.01.020.

[52] T. Munawar, S. Yasmeen, F. Mukhtar, M.S. Nadeem, K. Mahmood, M.S. Saif, M. Hasan, A. Ali, F. Hussain, F. Iqbal, $Zn_{0.9}Ce_{0.05}M_{0.05}O$ (M = Er, Y, V) nanocrystals: structural and energy bandgap engineering of ZnO for enhancing photocatalytic and antibacterial activity, Ceram. Int. 46 (2020) 14369–14383, https://doi.org/10.1016/j.ceramint.2020.02.232.

[53] J. Qiu, T.H. Nguyen, S. Kim, Y.J. Lee, M.T. Song, W.J. Huang, X.B. Chen, T.M. H. Nguyen, I.S. Yang, Two-dimensional correlation spectroscopy analysis of Raman spectra of NiO nanoparticles, Spectrochim. Acta A Mol. Biomol Spectrosc. 280 (2022) 121498, https://doi.org/10.1016/j.saa.2022.121498.

[54] H. Abbas, K. Nadeem, A. Hassan, S. Rahman, H. Krenn, Enhanced photocatalytic activity of ferromagnetic Fe-doped NiO nanoparticles, Optik 202 (2020) 163637, https://doi.org/10.1016/j.ijleo.2019.163637.

[55] J.A. Boukhari, M. Noun, R. Awad, Raman spectroscopic investigations of pure, (Mg, Cu), and (Mg, Ru) codoped NiO nanoparticles, Chem. Phys. Lett. 836 (2024) 141038, https://doi.org/10.1016/j.cplett.2023.141038.

[56] J. Qiu, T.H. Nguyen, Y.J. Lee, S. Kim, S.J. Kim, M.T. Song, W.J. Huang, X.B. Chen, I.S. Yang, Strong oxygen-content dependence of the magnetic excitations in antiferromagnetic NiO nanoparticles: a Raman probe, Spectrochim. Acta A Mol. Biomol Spectrosc. 297 (2023) 122700, https://doi.org/10.1016/j.saa.2023.122700.

[57] P. Mallick, C. Rath, J. Prakash, D.K. Mishra, R.J. Choudhary, D.M. Phase, A. Tripathi, D.K. Avasthi, D. Kanjilal, N.C. Mishra, Swift heavy ion irradiation induced modification of the microstructure of NiO thin films, Nucl. Instrum. Methods Phys. Res. Sect. B Beam Interact. Mater. Atoms (2010) 1613–1617, https://doi.org/10.1016/j.nimb.2010.02.005.

[58] C. Muiva, E. Muchuweni, D.P. Sebuso, T.K. Matabana, M. Thobega, H. Vasco, Microstructural analysis and optical linearity and nonlinearity of nanostructured Al— doped ZnO/SnO2 thin films, Cryst. Res. Technol. 60 (3) (2025) 2400118, https://doi.org/10.1002/crat.202400118, 2025.

[59] S.A. Benseghier, F. Bennabi, I. Ercan, H. Nehmar, Y. Khane, N. Moulayat, F. Ercan, T. Kayed, M. Adjdir, Low-Cost synthesis of Ag-doped NiO thin Films: their structural, optical, photocatalytic and antimicrobial properties, Inorg. Chem. Commun. 159 (2024) 111787, https://doi.org/10.1016/j.inoche.2023.111787.

[60] [60] R.G. Singh, H. Gupta, R.M. Mehra, F. Singh, Tuning of defects induced visible photoluminescence by swift heavy ion irradiation and thermal annealing in zinc

oxide films, Radiat. Phys. Chem. 183 (2021) 109400, https://doi.org/10.1016/j.radphyschem.2021.109400.
[61] Z.N. Kayani, B. Amir, S. Riaz, N. S, Antibacterial, magnetic, optical and dielectric analysis of novel La2O3 doped ZnO thin films, Opt. Mater. 109 (2020) 110287 1–9, https://doi.org/10.1016/j.optmat.2020.110287.
[62] A. Moumen, B. Hartiti, E. Comini, Z. El khalidi, H.M.M. Munasinghe Arachchige, S. Fadili, P. Thevenin, Preparation and characterization of nanostructured CuO thin films using spray pyrolysis technique, Superlattice. Microst. 127 (2019) 2–10, https://doi.org/10.1016/j.spmi.2018.06.061.
[63] K.N. Manjunatha, S. Paul, Investigation of optical properties of nickel oxide thin films deposited on different substrates, Appl. Surf. Sci. 10–15 (2015) 352, https://doi.org/10.1016/j.apsusc.2015.03.092.
[64] K. Lefatshe, P. Dube, D. Sebuso, M. Madhuku, C. Muiva, Optical dispersion analysis of template assisted 1D-ZnO nanorods for optoelectronic applications, Ceram. Int. 47 (2021) 7404–7415, https://doi.org/10.1016/j.ceramint.2020.11.079.
[65] A.K. Jokar, S. Torabi, M. Mirzaei, F. Dabir, F. BakhtiarGonbadi, H. Esfahani, Arrangement of n-type ZnO and p-type NiO nanofibrous thin films on FTO electrode for electrochemical impedance spectroscopy of glucose biosensors, Surf. Interfaces (2024) 105714, https://doi.org/10.1016/j.surfin.2024.105714.
[66] S. Elmassi, M. Beraich, M. Bousseta, A.E. Mouncharih, L. Amiri, S. Drissi, A. Abali, L. Nkhaili, A. Narjis, A.E. Kissani, A. Alsaad, A. Outzourhit, Theoretical and experimental investigations of the effect of cobalt doping on the structural, optical and electrical properties of sputtered NiO films for optoelectronic applications, Opt. Mater. 145 (2023) 114449, https://doi.org/10.1016/j.optmat.2023.114449.
[67] M. Sumathi, A. Prakasam, P.M. Anbarasan, Fabrication of hexagonal disc shaped nanoparticles g-C_3N_4/NiO heterostructured nanocomposites for efficient visible light photocatalytic performance, J. Cluster Sci. 30 (2019) 757–766, https://doi.org/10.1007/s10876-019-01535-6.
[68] A.A.A. Ahmed, E.A.A. Alahsab, A.M. Abdulwahab, The influence of Zn and Mg doping on the structural and optical properties of NiO nano-structures for optoelectronic applications, Results Phys. 22 (2021) 103938, https://doi.org/10.1016/j.rinp.2021.103938.
[69] A. Masood, N. Afzal, A.A. Ahmed, F.T. Qahtan, M. Rafique, R. Ahmad, M. Imran, Structural, surface and optical investigations of Cu^+ implanted NiO film prepared by reactive sputtering, Ceram. Int. 49 (2023) 4435–4448, https://doi.org/10.1016/j.ceramint.2022.09.330.
[70] S. Sorieul, J.M. Costantini, L. Gosmain, G. Calas, J.J. Grob, L. Thomé, Study of damage in ion-irradiated α-SiC by optical spectroscopy, J. Phys.: Condens. Mater. 18 (2006) 8493, https://doi.org/10.1088/0953-8984/18/37/008.
[71] E.A. Davis, N. Mott, Conduction in non-crystalline systems V. Conductivity, optical absorption and photoconductivity in amorphous semiconductors, Philosophical magazine: a J, Theoretical Experimental Appl. Phys. 22 (179) (1970) 903–922, https://doi.org/10.1080/14786437008221061.
[72] H.M. Gomaa, I.S. Yahia, H.Y. Zahran, Correlation between the static refractive index and the optical bandgap: review and new empirical approach, Physica B: Phys. Condens. Matter 620 (2021) 413246, https://doi.org/10.1016/j.physb.2021.413246.
[73] V.P. Gupta, N.M. Ravindra, Comments on the moss formula, Phys. Status Solidi (b) 100 (2) (1980) 715–719, https://doi.org/10.1002/pssb.2221000240.
[74] T.S. Moss, Relations between the refractive index and energy gap of semiconductors, Phys. Status Solidi (b) 131 (1985) 415, https://doi.org/10.1002/pssb.2221310202.
[75] A. Diha, S. Benramache, B. Benhaoua, Transparent nanostructured Co doped NiO thin films deposited by sol–gel technique, Optik 172 (2018) 832–839, https://doi.org/10.1016/j.ijleo.2018.07.062.
[76] L. Hannachi, N. Bouarissa, Band parameters for cadmium and zinc chalcogenide compounds, Physica B 404 (2009) 3650–3654, https://doi.org/10.1016/j.physb.2009.06.046.
[77] Y. Akaltun, T. Çayır, Fabrication and characterization of NiO thin films prepared by SILAR, J. Alloys Compd. 625 (2015) 144–148, https://doi.org/10.1016/j.jallcom.2014.10.194.
[78] Y. Chen, Y. Sun, X. Dai, B. Zhang, Z. Ye, M. Wang, H. Wu, Tunable electrical properties of NiO thin films and p-type thin-film transistors, Thin Solid Films 592 (2015) 195–199, https://doi.org/10.1016/j.tsf.2015.09.025.
[79] A.A. Ahmed, M.R. Hashim, M. Rashid, Control of the structural, electrical and optical properties of spin coated NiO fIms by varying precursor molarity, Thin Solid Films 690 (2019) 137554, https://doi.org/10.1016/j.tsf.2019.137554.
[80] H. Sun, S.C. Chen, S.W. Hsu, C.K. Wen, T.H. Chuang, X. Wang, Microstructures and optoelectronic properties of nickel oxide films deposited by reactive magnetron sputtering at various working pressures of pure oxygen environment, Ceram. Int. 43 (2017) S369–S375, https://doi.org/10.1016/j.ceramint.2017.05.242.